

Chiral Mott phase of three-component fermions on the triangular lattice

C. Boos,^{1,2,*} M. Lajkó,^{2,†} P. Nataf,^{3,‡} K. Penc,^{4,5,§} K. P. Schmidt,^{1,¶} and F. Mila^{2,**}

¹*Institute for Theoretical Physics, FAU Erlangen-Nürnberg, Germany*

²*Institute of Physics, Ecole Polytechnique Fédérale de Lausanne (EPFL), CH 1015 Lausanne, Switzerland*

³*Univ. Grenoble Alpes, CEA INAC-PHELIQS, F-38000, Grenoble, France*

⁴*Institute for Solid State Physics and Optics, Wigner Research Centre for Physics,
Hungarian Academy of Sciences, H-1525 Budapest, P.O.B. 49, Hungary*

⁵*MTA-BME Lendület Magneto-optical Spectroscopy Research Group, 1111 Budapest, Hungary*
(Dated: August 30, 2022)

We provide numerical evidence in favor of spontaneous chiral symmetry breaking in the Mott phase of three-component fermions on the triangular lattice, that we describe by an $SU(3)$ symmetric Hubbard model with hopping t and on-site interactions U . Our approach relies on effective models derived in the strong-coupling limit in powers of t/U for general $SU(N)$ and arbitrary flux, which are studied using exact diagonalization and variational Monte Carlo simulations for $N = 3$. Up to third order in t/U , there is a large chiral phase that encompasses a range of real ring exchange where time-reversal is spontaneously broken. For the Hubbard model, this phase is stabilized below $U/t \simeq 13$, as revealed by including higher-order effects. How to realize it with ultra cold atoms without artificial gauge fields is briefly discussed.

Quantum spin liquid phases are unconventional states of matter that have gained a lot of attention in the last decades due to their fascinating properties and possible applications in quantum devices like quantum computers [1]. From a theoretical point of view they are expected to emerge in strongly-correlated systems, for instance in Mott insulating phases. The recent progress in experiments with ultra cold atoms in optical lattices opens the exciting new possibility to simulate a broad variety of such quantum models [2]. The optical lattice allows one to adjust the lattice type as well as the interaction strength, which can be enlarged sufficiently to reach the Mott phase [3–5]. Furthermore, a synthetic gauge field (the analog of magnetic flux in electronic systems) can be imposed [6, 7]. The fundamental degrees of freedom can be adjusted by the choice of atom type. In particular fermionic alkaline rare earth atoms provide an $SU(N)$ symmetric spin degree of freedom with $N \leq 10$, because of an almost perfect decoupling between nuclear spin and electronic angular momentum [8–12]. This new possibility to realize $SU(N)$ symmetric Hubbard models within the Mott phase [4, 5] creates a strong motivation for further theoretical investigations to name potential realistic hosts of quantum spin liquid phases.

In this Letter, we focus on chiral spin liquids (CSL), which are defined by breaking parity and time-reversal symmetry, but not their product [13]. For $SU(2)$, a CSL has been recently discovered for the spin-1/2 Heisenberg kagome antiferromagnet when specific values of second and third neighbor interactions are considered [14–16]. For $SU(N)$, CSL phases were first discovered in a large N limit on the square lattice [13, 17]. For $SU(3)$ symmetric fermions on the frustrated triangular lattice a number of studies were performed for the J - K model [18–21]. This spin model includes nearest-neighbor Heisenberg interaction J as well as three-site ring exchange K on ev-

ery triangle. Besides the conventional three-sublattice long-range ordered (3-SL LRO) phase [22, 23], a $d_x + id_y$ CSL with spontaneous time-reversal symmetry breaking was predicted by variational Monte Carlo (VMC) for real $K \gtrsim 0.6$ [18]. However the uniform $\pi/3$ -flux and $2\pi/3$ -flux CSL states were not considered and a later mean-field study found that they are favored energetically for $0.41 \lesssim K \lesssim 6.0$ and $K \gtrsim 6.0$ respectively [20]. For the J - K model with purely imaginary ring exchange, hence explicitly broken time-reversal symmetry, the presence of CSL phases has been confirmed for all $2 < N < 10$ by exact diagonalization (ED) and VMC [21]. However, whether this phase exists for the full range of complex ring exchanges, including the most interesting case of real ring exchange where the time-reversal symmetry would be spontaneously broken, is not known. Besides, with respect to experiments, the most relevant open question is whether the CSL phases are also present in the $SU(3)$ Hubbard model, for which the J - K model only provides a reliable description at very strong coupling.

The $SU(N)$ Hubbard model with uniform flux is defined by the Hamiltonian

$$\mathcal{H} = -t \sum_{\langle i,j \rangle} \sum_{\alpha=1}^N (e^{i\phi_{ij}} c_{i\alpha}^\dagger c_{j\alpha} + \text{h.c.}) + U \sum_{i,\alpha < \beta} n_{i\alpha} n_{i\beta} \quad (1)$$

where the phases ϕ_{ij} around each triangle add up to the flux Φ . In the strong-coupling limit with an average of one particle per site the system is in a Mott insulating phase, and the effective description up to third-order in t/U is given by the J - K model defined by the Hamiltonian

$$\mathcal{H} = J \sum_{\langle i,j \rangle} P_{ij} + \sum_{\langle i,j,k \rangle} (K P_{ijk} + \text{h.c.}) \quad (2)$$

where the first sum runs over all nearest neighbor sites, the second sum over all triangles of the lattice, the trans-

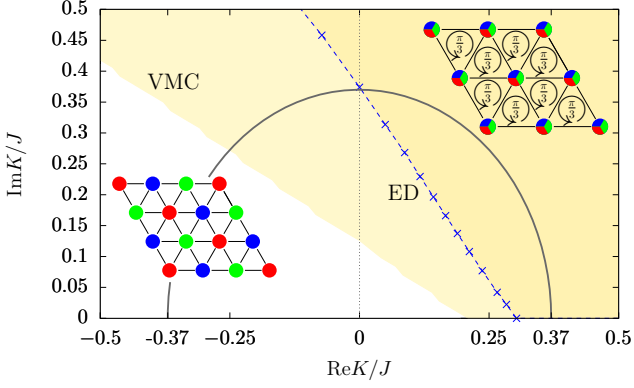


FIG. 1. Phase diagram of the J - K model for complex phases between zero and π . White phase: 3-SL LRO according to VMC on 36 sites. Yellow phase: CSL according to VMC (light and dark) and ED (dark). The blue crosses show the phase transition induced from the level crossing of the excited states in the 21-site cluster ED. The gray semi-circle indicates the path of the energy spectrum shown in Fig. 2.

position operator P_{ij} exchanges the states on sites i and j , and the operator P_{ijk} is a ring exchange operator that cyclically permutes the states on the sites i, j , and k . The coupling constants are $J = 2t^2/U - 12 \cos(\Phi) t^3/U^2$ and $K = -6e^{i\Phi} t^3/U^2$. We assume $J > 0$ in what follows.

The phase diagram of this model is shown in Fig. 1 for $|K|/J \leq 0.5$ and complex phases of the three-site ring exchange $\varphi \in [0, \pi]$. At this order, the complex phase equals the flux through an elementary plaquette in the Hubbard model. This phase diagram has been determined using two independent numerical methods: (i) ED on clusters with periodic boundary conditions (PBC) on 12 and 21 sites exploiting the full $SU(3)$ symmetry [24]. The symmetry sectors correspond to irreducible representations (irreps) of $SU(N)$ described by Young tableaux; (ii) VMC calculations of different Gutzwiller projected fermionic parton wave functions [25–27], a method known to be efficient in identifying spin liquid phases [21, 28, 29]. We considered multiple color and plaquette ordered phases, as well as chiral liquid phases with various fluxes per triangular plaquette in the tight-binding model [13, 19, 20]. A detailed list of the considered scenarios and variational parameters is given in the Supplementary Material. We carried out these calculations on a 36-site system as some of the variational hopping configurations are incompatible with the 21-site cluster. We then made calculations on 21 sites for the energetically most favored states including higher order interactions and considering the overlap between variational states with different twisted boundary conditions [21, 30, 31] to offer a better comparison with ED results.

According to both methods, for small $|K|/J$ the 3-SL LRO [22, 23] is present for all values of φ shown as

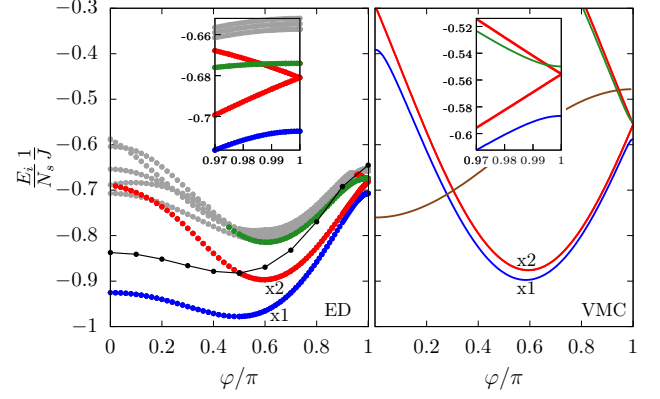


FIG. 2. Energy spectrum of the J - K model as a function of φ for fixed $|K|/J = 0.37$ on a 21-site cluster. Left panel: ED. The energies from the eight-dimensional irrep **8** are shown in black. All other colors belong to the singlet sector **1**. Right panel: VMC. The 3-SL LRO state is shown in brown, all other states represent chiral states. The colors of the chiral states keep track of the degeneracies and symmetries. They are given explicitly in the Supplementary Material.

white area in Fig. 1. It dominates the phase diagram for ferromagnetic ring exchange with $\text{Re}K/J < 0$ as long as $\text{Im}K/J$ is not too strong. For the purely imaginary case a phase transition to the $\pi/3$ -flux CSL phase (yellow area) emerges [21]. We find that this CSL remains stable for a wide range of phases including the purely real case at $\varphi = \pi$, where the model is symmetric under time-reversal.

The logic we used to map out the phase diagram is best explained by following a characteristic energy spectrum with constant $|K|/J = 0.37$ (gray semi-circle in Fig. 1). The evolution of the spectrum as a function of φ is shown in Fig. 2 both for ED (left) and VMC (right). For small values of the phase φ , the ground state in ED lies in the singlet sector (blue circles), whereas the first excited state (black circles) belongs to the irrep **8**. This signals a tower of states that occurs in long-range ordered phases [32, 33]. Since this signature is adiabatically connected to the Heisenberg point $K = 0$, we identify this part of the phase diagram with 3-SL LRO [22, 23, 33]. This ordered phase extends up to $\varphi \approx \pi/2$, where the spectrum exhibits a level crossing of the first excited state so that the first excitation (red circles) lies in the singlet sector and is two-fold degenerate for larger values of $\varphi < \pi$. As a consequence, a manifold of three low-lying states emerges consisting of the non-degenerate ground state (blue circles) and this two-fold degenerate first-excited state (red circles). On a torus, this is characteristic of a topologically ordered CSL when time-reversal symmetry is explicitly broken [13]. We therefore use the presence of these three low-energy states as the indicator for such a CSL in ED. For the specific case $\varphi = \pi/2$, the same CSL has been found in Ref. [21]. The fidelity of this

identification depends on the energy splitting within the manifold compared to the energy gap to the other excited states, which is a consequence of the finite cluster size. On the 21-site cluster, the splitting of the manifold becomes smaller and the energy gap to higher excited states becomes larger with increasing values of $\varphi > \pi/2$ deeper in the CSL phase. A quantitative finite-size scaling cannot be performed since larger clusters are currently not within reach with ED. Nevertheless, the comparison with the smaller 12-site cluster confirms our identification of the CSL: the splitting is larger and the gap smaller (see Supplementary Materials). Finally, we discuss the particularly important case $\varphi = \pi$ where time-reversal symmetry is not explicitly broken. Here we observe a manifold of six low-lying states, since another set of three states drops down close to $\varphi = \pi$. These three states are exactly the time-reversal counterparts of the three-fold manifold present for $\varphi < \pi$. The resulting six low-energy states consist of a non-degenerate ground state (blue circles), a four-fold degenerate first-excited state (red circles), and a non-degenerate second-excited state (green circles).

These findings are fully confirmed by VMC, which gets the same sequence of ground states, i.e. 3-SL LRO (brown line) for $0 \leq \varphi \lesssim 0.28\pi$ and a CSL (blue, red and green lines) for larger values of the flux. We note that the critical phase 0.28π is smaller than in ED which is due to the fact that the 3-SL LRO state is captured less accurately within the VMC. However, the low-energy states show the same degeneracies and symmetries in VMC and ED. This holds in particular for the three-fold manifold of the CSL for $\varphi < \pi$ as well as for the six-fold manifold at $\varphi = \pi$ where time-reversal symmetry is spontaneously broken. The ground-state phase diagrams of ED and VMC therefore agree in all qualitative aspects for the J - K model. In particular they both indicate the presence of a CSL with spontaneous breaking of time-reversal symmetry.

Next we turn to the question whether the above findings are also present in the Mott phase of the corresponding Hubbard model (1). Most importantly, we aim at clarifying if the Hubbard model realizes a CSL where time-reversal symmetry is spontaneously broken. We therefore focus on the case $\Phi = \pi$ along the antiferromagnetic line of the model. In the limit of small values of t/U the Mott phase is well described by the leading nearest-neighbor Heisenberg model stabilizing the 3-SL LRO. With increasing t/U , the next subleading interaction, the third-order K -term, triggers a phase transition to the CSL for large enough fluxes. At $\Phi = \pi$ the ED critical value is $K/J \approx 0.31$, corresponding to $t/U \approx 0.064$ taking the bare third-order series. In the following we show that higher-order contributions do not prevent the occurrence of the CSL phase at $\Phi = \pi$, and that the critical value remains similar.

First, let us explain the derivation and the nature of the effective model for the Mott phase of a general $SU(N)$

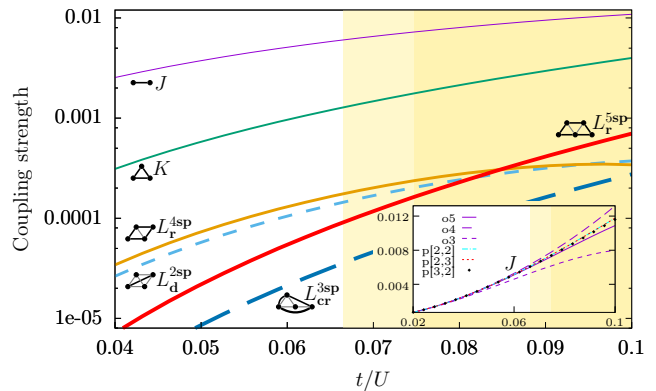


FIG. 3. Effective couplings in units of U of the Hubbard model as a function of t/U for $\Phi = \pi$ using bare fifth-order series. Plotted are the largest contributions in every order with a pictogram sketching the associated permutations. The inset shows the nearest-neighbor exchange in different orders and Padé extrapolations. The dark yellow background indicates the area where the CSL is observed within ED and VMC, whereas the light yellow corresponds to its stability according to VMC only.

Hubbard model at a commensurate $1/N$ filling. To this end we perform perturbation theory about the strong-coupling limit $t = 0$ where unperturbed ground states correspond to all product states with exactly one particle per site. The degeneracy of these states is N^n with the number of sites n . The quantum fluctuations are induced by the hopping part of the Hubbard model which is treated as a perturbation. Technically, we exploit the linked-cluster theorem using white graphs [34] and we perform degenerate perturbation theory on finite linked clusters [35–39]. A link between two sites of a cluster is created by the perturbation, which physically corresponds to a hopping of a fermion on these sites. A finite cluster is called linked when each site of the cluster is connected with all other sites via a set of links. We find that in order k only linked clusters with up to k sites contribute which restricts the maximum number of colors to k . Therefore, in order k , only $N \leq k$ has to be considered for the derivation of the effective model for all N . The resulting exchange interactions on each linked cluster are then embedded in the infinite system yielding the effective low-energy model in the thermodynamic limit. The detailed derivation can be found in the Supplementary Materials.

We determined the effective low-energy $SU(N)$ model up to order five in t/U for arbitrary fluxes Φ . The effective Hamiltonian in its generic form can be expressed with permutation operators acting on all possible sets of sites in units of U as

$$H_{\text{eff}}(t/U, \Phi) = \sum_{(i,j)} A_{ij} P_{ij} + \sum_{(i,j,k)} B_{ijk} P_{ijk} + \dots, \quad (3)$$

where the coupling constants depend on t/U and Φ . In fifth-order perturbation theory the effective description contains 13 different types of exchange interactions involving permutations on up to five sites (see Supplementary Materials).

Next we analyze (3) for the specific case $N = 3$ on the triangular lattice. For small t/U the couplings up to third order are dominant, hence the J - K model is well converged. With increasing t/U the convergence depends non-trivially on the flux Φ . Whenever possible, we have performed Padé extrapolations [40] of the coupling constants A_{ij} , B_{ijk} , ... to enhance the validity range of the effective model (3) (see Supplementary Materials). The convergence of the series and the associated extrapolation works particularly well for the most interesting case $\Phi = \pi$. The largest coupling constants of the effective model for that case are shown order by order as a function of t/U in Fig. 3. The most important subleading corrections to the nearest-neighbor Heisenberg term correspond to ring exchanges around triangles, squares, and 5-site trapezoids. For $\Phi = \pi$ the phase transition in the J - K model occurs at $|K|/J \approx 0.31$ which translates to $t/U \approx 0.09$ in bare fifth-order. Interestingly, this critical value changes only slightly to $t/U \approx 0.1$ when applying Padé extrapolations to the couplings J and K (see Supplementary Materials). For both couplings several Padé extrapolants give essentially the same result in this t/U -regime so that the extrapolations work well for the most important interactions of the effective model (see also the inset in Fig. 3). The small difference between the critical ratios from bare series and extrapolation within the J - K model indicates that even the bare series is almost converged up to these t/U values for the couplings J and K .

Since the impact of all the other smaller terms is not obvious a priori, we study the effective fifth-order model explicitly using ED and VMC. The energy spectrum of the full effective model for flux $\Phi = \pi$ on the 21-site cluster is shown in the right panel of Fig. 4. As expected, the signature of a tower of states in ED and a 3-SL LRO ground state in VMC are present for small values of t/U . More importantly, we detect the same manifold of six low-lying states with respect to degeneracies and symmetries for $t/U \gtrsim 0.075$ (or equivalently $U/t \lesssim 13$) as in the J - K model shown in the left panel of Fig. 4. These findings point to the existence of a CSL phase with spontaneous breaking of time-reversal symmetry in the SU(3) Hubbard model on the triangular lattice. The manifold of six low-lying states is not very well separated from the excited states in ED, but the tendency between 12 and 21 sites is clear. The low-energy spectra exhibit similar states, but on the 12-site cluster the manifold of six states is intertwined by an excited state in contrast to the 21-site cluster (see Supplementary Materials). Hence, increasing the system size strengthens the signature of the CSL phase, as for the J - K model.

Let us discuss our findings for the specific case $\Phi = \pi$ in the context of the full phase diagram. The quality of convergence depends non-trivially on the flux and we do not find a convincing convergence around $\Phi \approx 0.75\pi$. This comes from cancellation effects between different perturbative orders: a lower-order term can be strongly suppressed as compared to a higher-order one for certain values of Φ and t/U . In contrast, there is a suitable convergence around $\Phi = \pi/2$ and $\Phi = \pi$, and we found good evidence of a CSL in both cases. We thus expect that the Mott phase of the SU(3) Hubbard model on the triangular lattice realizes the same quantum phases and phase transitions as the ones found for the J - K model in Fig. 1.

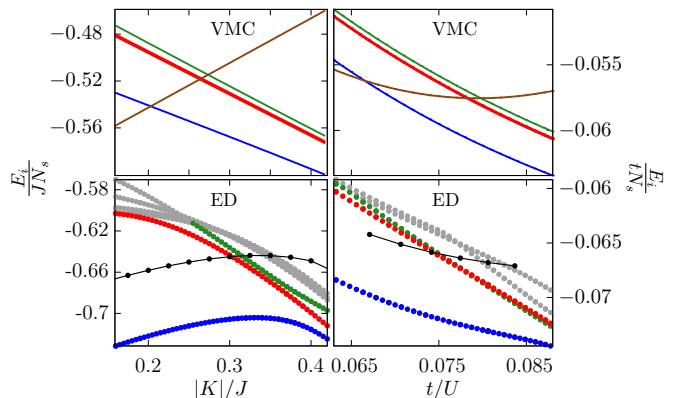


FIG. 4. Energy spectrum of the J - K model for $\varphi = \pi$ as a function of $|K|/J$ (left), and energy spectrum of the full effective spin model as a function of t/U for $\Phi = \pi$ (right) from ED and VMC on the 21-site cluster. As in Fig. 2, we identify two phases: i) 3-SL LRO, when the first excitation belongs to the irrep **8** (black circles) in ED, or when the 3-SL ordered variational state (brown line) is the lowest in energy in VMC; ii) a CSL, when the first excited states in ED are singlets (red and green), or when the VMC ground state has a non-zero flux (blue). In the CSL, there are six low-lying chiral states in total, as it should: a fourfold degenerate one (red) and two non-degenerate ones (blue and green).

Regarding cold atom experiments, we note that the most interesting case $\Phi = \pi$ realizing the CSL with spontaneous breaking of time-reversal symmetry is also the most accessible experimentally since it does not require an artificial gauge field. The only potential problem is the sign of the hopping term. With the convention of Eq. (1), K/J is positive if t is negative. However, if $t > 0$, a particle-hole transformation maps the SU(3) Hubbard model at filling $2/3$ to the Hubbard model at a filling $1/3$ with the opposite sign of t . So, in that case, the CSL will be accessible in the Mott phase with two fermions per site, realizing the **3** antifundamental irrep at each site. The experimental observation of such a CSL is therefore within reach with existing technology using ultra cold alkaline rare earth atoms in optical lattices.

We thank Andreas Läuchli for useful discussion. We

acknowledge financial support by the German Science Foundation (DFG) through the Engineering of Advanced Materials Cluster of Excellence (EAM) at the Friedrich-Alexander University Erlangen-Nürnberg (FAU), by the Hungarian NKFIH Grant No. K124176, and by the Swiss National Science Foundation. The calculations have been performed using the facilities of the Scientific IT and Application Support Center of EPFL and of the Erlangen Regional Computing Center (RRZE).

Supplementary Materials to "Chiral Mott phase of three-component fermions on the triangular lattice".

C. Boos, M. Lajkó, P. Nataf, K. Penc, K. P. Schmidt, and F. Mila

The first parts of these Supplementary Materials give a detailed description of the derivation of the effective model and its properties like the convergence as well as ED on finite clusters. The final parts give details about the VMC states on the 36-site cluster and give additional information on the chiral states.

DERIVATION OF THE EFFECTIVE MODEL

The effective model is derived by a linked-cluster expansion (LCE), where all contributing clusters are studied with degenerate perturbation theory. In the following we explain the basic idea of the LCE and define the main steps of the perturbation theory before giving detailed information about the derivation of the fifth-order effective $SU(N)$ -Hubbard model for an average filling of one particle per site in the strong-coupling limit. A similar approach was successfully applied to the $SU(2)$ -Hubbard model in [39].

A LCE is a technique to extend results on finite clusters to the thermodynamic limit. Let us consider a generic problem on an arbitrary lattice in the thermodynamic limit and an extensive quantity P . Then the ratio P/n with the number of lattice sites n is given by a weighted sum over all topological different clusters c

$$\frac{P}{n} = \sum_c L(c) W_P(c). \quad (S1)$$

The multiplicity $L(c)$ is the number of ways in which a cluster can be embedded on the infinite lattice and determines the impact of each cluster. The weight of a cluster $W_P(c)$ to the property P is given by the inclusion-exclusion principle. This means that only reduced contributions appearing on the considered cluster but not on its subclusters are taken into account

$$W_P(c) = P(c) - \sum_{s \subset c} W_P(s). \quad (S2)$$

One calculates the physical property $P(c)$ on cluster c and subtracts the weights of all subclusters s . Evidently, all processes on a disconnected cluster are already included in the sum of its pieces and their weights vanish. Therefore, only linked clusters contribute and the weight of a cluster contains only properties that arise from all bonds of the cluster. This fact can be used to calculate the weights directly with a white-graph expansion [34], which makes the subtraction unnecessary. In the form of Eq. (S1) the LCE includes every contribution of linked clusters on the full lattice via an infinite sum and is not perturbative. If one applies it though, one has to find a way to truncate the series.

On every linked-cluster we use degenerate perturbation theory, which was first applied in the context of the half-filled Hubbard model at low temperature in 1977 by Takahashi [36]. We consider a general Hamiltonian H which is acting on the Hilbert space \mathcal{H} . The Hamiltonian is split up into two parts

$$H = H_0 + V, \quad (S3)$$

such that the first part H_0 has degenerate ground states defined in the subspace \mathcal{H}_0 of \mathcal{H} with the eigenenergy E_0 and the perturbation V . The goal is to find an effective Hamiltonian H_{eff} describing H for small perturbations, which is defined in the subspace \mathcal{H}_0 by an isometric linear transformation of the form

$$H_{\text{eff}} = \Gamma^\dagger H \Gamma, \quad (S4)$$

with the transformation matrix Γ . The formal construction of this matrix is derived in Takahashi's paper up to infinite orders in terms of a projection operator P into the subspace \mathcal{H}_0 and a resolvent operator $S = (1 - P)/(H_0 - E_0)$. Here we give the effective Hamiltonian in third-order to illustrate what kind of calculations are required

$$H_{\text{eff}}^{O(3)} = PH_0P + PVP + PVSVP + PVSVP - \frac{1}{2}PVPVS^2VP - \frac{1}{2}PVS^2VPVP. \quad (S5)$$

The effective Hamiltonian consists of terms with combinations of perturbation V , projection P and resolvent operators S , wherein the projections enclosing each term ensure that the effective model is defined in \mathcal{H}_0 .

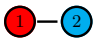
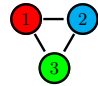
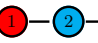
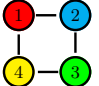
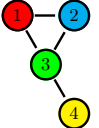
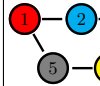
dimer	triangle	trimer	four-site loop	triangle plus one site	five-site loop
					
second-order	third-order	fourth-order	fourth-order	fifth-order	fifth-order

TABLE I. All relevant graphs for the effective model in order five with the associated order in which they first yield contributing exchanges after subtraction.

For the $SU(N)$ -Hubbard model with a uniform flux Φ in the strong-coupling limit the unperturbed Hamiltonian H_0 is given by the Hubbard interaction that is $t \rightarrow 0$ in Eq. (1) of the main article. In the following we always give effective Hamiltonians and effective couplings in units of U . Considering an average filling of one particle per site the ground state subspace \mathcal{H}_0 is spanned by all states without multiple occupied sites, namely pure spin states. The hopping term is then taken into account as the perturbation V . When V is applied on a ground state it always leads to an excited state with one double occupied site. As a first simple conclusion all terms including PVP in the transformation vanish. All relevant linked-clusters in the LCE are determined by the following condition. A linked-cluster contributes to the LCE, if the number of links that are part of a loop plus twice the number of links that are not part of a loop is smaller than the order. The factor two arises because a single hopping on a link that is not part of a loop leads to an excited state and the contribution vanishes after projection P . For example, the linked-cluster of a triangle plus an additional site starts to contribute only in order five.

On a finite cluster for arbitrary N , that is possibly larger than the number of sites n , the basis of spin states consists of all states with maximal n different spin colors. Actually, the cases where $N < n$ are all included within the case $N = n$ and one has to consider only a basis of $N!$ states for every linked-cluster.

In this work we use a very appealing LCE approach along the lines of a white-graph expansion [34], which originally was set up to reduce the number of separate linked-cluster calculations. Here we use it to simplify the subtraction process, as well as to include complex phases. To this end, every bond on a linked-cluster is labeled with a different exchange constant during the calculation. For instance, on the triangle we take three exchange constants h_1 , h_2 and h_3 connecting different sites. The perturbation is written as

$$V_{\text{triangle}} = \sum_{\alpha=1}^3 \left(h_1 c_{1\alpha}^\dagger c_{2\alpha} + h_2 c_{2\alpha}^\dagger c_{3\alpha} + h_3 c_{3\alpha}^\dagger c_{1\alpha} \right) + \text{h.c.}$$

The subtraction of the so derived effective Hamiltonian is then achieved by taking only terms that include every exchange constant at least once and hence emerge from perturbations that link the whole cluster. This procedure can be extended to include complex phase factors by splitting up the hopping process on a link into the hopping from left to right and from right to left. For the triangle one can choose

$$V_{\text{triangle}} = \sum_{\alpha=1}^3 \left(h_{1A} c_{1\alpha}^\dagger c_{2\alpha} + h_{1B} c_{1\alpha}^\dagger c_{2\alpha} \right) + \sum_{\alpha=1}^3 \left(h_{2\alpha} c_{2\alpha}^\dagger c_{3\alpha} + h_{3\alpha} c_{3\alpha}^\dagger c_{1\alpha} \right) + \text{h.c.}$$

The complex phase can then be included by setting $h_{1A} = h_1 e^{i\Phi} = h_{1B}^*$.

In order five on the triangular lattice six linked-clusters give a non-zero contribution, namely the dimer, the trimer, the triangle, a triangle with one additional site, a four-site and a five-site loop. They are all depicted in Tab. I. For each cluster one derives the associated effective Hamiltonian, where we perform the subtraction directly as described above. These Hamiltonians can already be written in a compact form with permutation operators P_{ij} interchanging the spins on sites i and j . For instance the effective subtracted Hamiltonian of the triangle in order three is

$$\tilde{H}_{\text{eff, triangle}}^{O(3)} = \tilde{A}_{\text{triangle}} + \tilde{B}_{\text{triangle}} (P_{12} + P_{23} + P_{13}) + \tilde{C}_{\text{triangle}} P_{12} P_{23} + \tilde{C}_{\text{triangle}}^* P_{32} P_{21}$$

with the parameters

$$\tilde{A}_{\text{triangle}} = -6 \frac{t^3}{U^3} \cos(\Phi), \quad \tilde{B}_{\text{triangle}} = 6 \frac{t^3}{U^3} \cos(\Phi) \quad \text{and} \quad \tilde{C}_{\text{triangle}} = -6 e^{i\Phi} \frac{t^3}{U^3}.$$

Every linked-cluster yields a different set of exchanges that are embedded on the full infinite lattice in the second step. Some of these exchanges are unique to the specific cluster, e.g. the ring-exchange on the five-site loop in order

five. Here the embedding becomes trivial. Other interactions emerge from contributions of a variety of linked-clusters in the thermodynamic limit like the nearest-neighbor exchange. In third order it arises from the dimer with a single possibility for the embedding and the triangle, which possess two options to align with one edge to a single bond. The effective coupling constant in the thermodynamic limit then reads

$$B_{\text{NN}}^{\mathcal{O}(3)} = B_{\text{dimer}} + 2\tilde{B}_{\text{triangle}}.$$

Extending these calculations to order five for all appearing interactions leads to the effective model given in the next Section.

EFFECTIVE MODEL

The effective fifth-order model is given by the Hamiltonian

$$\begin{aligned}
H_{\text{eff}}^{\mathcal{O}(5)} = & E_0 + J \sum_{i-j} P_{ij} + \sum_{\substack{i-j \\ | \quad k}} (KP_{ijk} + \text{h.c.}) + L_s^{2\text{sp}} \sum_{i-\bullet-j} P_{ij} + L_d^{2\text{sp}} \sum_{\substack{i-j \\ | \quad \bullet}} P_{ij} \\
& + L_s^{3\text{sp}} \sum_{i-j-k} (P_{ijk} + \text{h.c.}) + \sum_{i-j \swarrow k} \left(L_d^{3\text{sp}} P_{ijk} + \text{h.c.} \right) + \sum_{\substack{i-j \\ | \quad l-k}} (L_r^{4\text{sp}} P_{ijkl} + \text{h.c.}) \\
& + \sum_{\substack{i-\bullet-j \\ | \quad k}} (L_{\text{cr}}^{3\text{sp}} P_{ijk} + \text{h.c.}) + \sum_{\substack{i-j-k \\ | \quad l}} (L_{\text{cr}}^{4\text{sp}} (P_{lijk} + P_{kjli}) + \text{h.c.}) + L_{\text{pl}}^{4\text{sp}} \sum_{\substack{i-j \\ | \quad l-k}} (P_{ikjl} + P_{kijl} + \text{h.c.}) \\
& + L_{\text{Ka}}^{4\text{sp}} \sum_{\substack{i-j \\ | \quad l-k}} P_{ij} P_{lk} + L_{\text{Kb}}^{4\text{sp}} \sum_{\substack{i-j-k \\ | \quad l}} P_{il} P_{jk} + \sum_{\substack{i-j-k \\ m-l}} (L_r^{5\text{sp}} P_{ijklm} + \text{h.c.}),
\end{aligned} \tag{S6}$$

where the pictogram underneath every sum indicates which sites on the full lattice are addressed. This has to be understood as follows. The indicated graphs are not allowed to be changed in the angles between links (e.g. the graph of L_d^{3sp} can not be transformed into that of L_s^{3sp}), however every possibility of rotation has to be included (e.g. the graph of L_d^{3sp} can be rotated around the axis defined by i and j by π). Then every distinct set of sites contributes to the Hamiltonian. Products of permutation operators are written in a short form when they act on the same site, for instance $P_{ijk} \equiv P_{ij}P_{jk}$. The prefactors are

$$\begin{aligned}
E_0 &= -6 \frac{t^2}{U^2} - 12 \cos(\Phi) \frac{t^3}{U^3} + (-26 - 24 \cos(2\Phi)) \frac{t^4}{U^4} - (92 \cos(\Phi) + 60 \cos(3\Phi)) \frac{t^5}{U^5}, \\
J &= 2 \frac{t^2}{U^2} + 12 \cos(\Phi) \frac{t^3}{U^3} + (12 + 40 \cos(2\Phi)) \frac{t^4}{U^4} + \left(\frac{820}{9} \cos(\Phi) + 140 \cos(3\Phi) \right) \frac{t^5}{U^5}, \\
K &= -6e^{i\Phi} \frac{t^3}{U^3} + (-4 - 30e^{i2\Phi}) \frac{t^4}{U^4} - \left(\frac{58}{3} e^{i\Phi} - 16e^{-i\Phi} + 135e^{i3\Phi} \right) \frac{t^5}{U^5}, \\
L_s^{2\text{sp}} &= \frac{10}{3} \frac{t^4}{U^4} + \left(\frac{104}{3} \cos(\Phi) + 20 \cos(3\Phi) \right) \frac{t^5}{U^5}, \\
L_d^{2\text{sp}} &= \left(\frac{20}{3} + 8 \cos(2\Phi) \right) \frac{t^4}{U^4} - \left(\frac{208}{3} \cos(\Phi) + 40 \cos(3\Phi) \right) x^5 \\
L_s^{3\text{sp}} &= -\frac{4}{3} \frac{t^4}{U^4} - \left(\frac{32}{3} \cos(\Phi) + 30 \cos(3\Phi) \right) \frac{t^5}{U^5}, \\
L_d^{3\text{sp}} &= \left(-\frac{4}{3} - 10e^{i2\Phi} \right) \frac{t^4}{U^4} - \left(\frac{32}{3} \cos(\Phi) + \frac{224}{9} e^{i\Phi} + 60e^{i3\Phi} \right) \frac{t^5}{U^5},
\end{aligned} \tag{S7}$$

$$\begin{aligned}
L_r^{4\text{sp}} &= 20e^{i2\Phi} \frac{t^4}{U^4} + \left(\frac{232}{9}e^{i\Phi} + 140e^{i3\Phi} \right) \frac{t^5}{U^5}, \\
L_{\text{cr}}^{3\text{sp}} &= - \left(\frac{112}{9}e^{i\Phi} + 15e^{i3\Phi} \right) \frac{t^5}{U^5}, \quad L_{\text{cr}}^{4\text{sp}} = \frac{58}{9}e^{i\Phi} \frac{t^5}{U^5}, \quad L_{\text{pl}}^{4\text{sp}} = \frac{116}{9}\cos(\Phi) \frac{t^5}{U^5}, \\
L_{\text{Ka}}^{4\text{sp}} &= -\frac{232}{9}\cos(\Phi) \frac{t^5}{U^5}, \quad L_{\text{Kb}}^{4\text{sp}} = -\frac{116}{9}\cos(\Phi) \frac{t^5}{U^5} \quad \text{and} \quad L_r^{5\text{sp}} = -70e^{i3\Phi} \frac{t^5}{U^5}.
\end{aligned} \tag{S8}$$

The representation of the effective model given above is not unique for real exchange constants if $N < 5$. This is due to the fact that consecutive permutations acting on more sites than spin colors in the model can be rewritten in terms of sums of various other permutation operators. The best known example occurs for the three-site permutation acting on SU(2) spins, which can be expressed by two-site permutations plus a constant. The situation becomes much richer if one considers permutations between more spins. For instance in the case of SU(3) spins the four-site permutation can be rewritten in terms of two-spin, three-spin and various four-spin interactions

$$P_{1234} + P_{4321} = 1 - \sum_{(i,j)} P_{ij} + \sum_{(i,j,k)} P_{ijk} - (P_{1243} + P_{1324} + \text{h.c.}) + P_{12}P_{34} + P_{14}P_{23} + P_{13}P_{24}, \tag{S9}$$

where the sums include all possible permutations of different sites. If we use this relation to reexpress the four-site ring exchange on a plaquette in the effective Hamiltonian all exchange constants of the exchanges appearing on the right hand side of Eq. (S9) get rescaled. Additionally, new interactions occur which in perturbation theory arise only in higher-orders. In this sense the replacement of operators is not helpful and the formulation in Eq. (S6) is the more natural one in terms of perturbation theory. If and how a systematical reduction of higher-order interactions to only already included exchanges is possible for orders larger than five remains an open question.

The convergence of the bare series can be improved using Padé extrapolations [40] denoted with $[m, n]$ where the degree of the numerator is m and that of the denominator is n . This was already shown for the most important nearest-neighbor coupling J for $\Phi = \pi$ in the inset of Fig. 3 of the main article. Here we give a similar plot for the subleading three-site ring exchange K displaying bare series and Padé extrapolations, as well as for the most relevant ratio K/J , where we take the ratio of the extrapolations of J and K , in Fig. S1. The Padé extrapolations

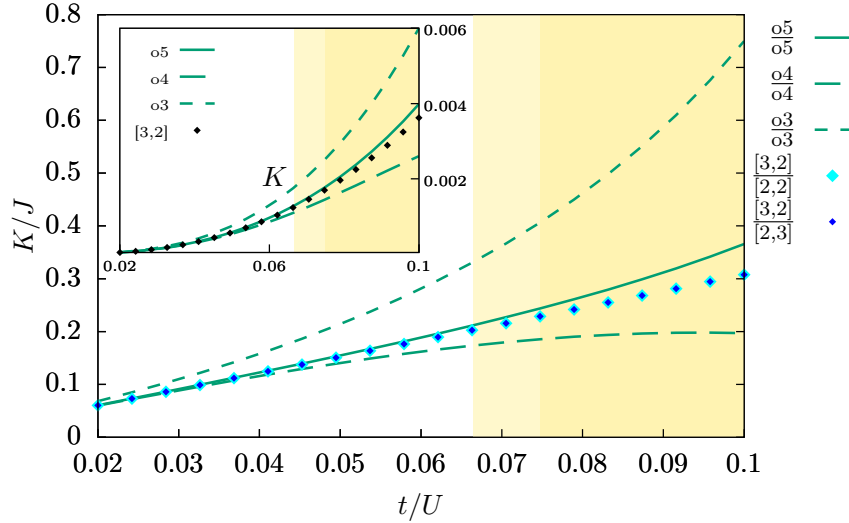


FIG. S1. Ratio of effective coupling constants K/J depending on t/U for $\Phi = \pi$ using bare series up to order five (green) as well as Padé extrapolations (cyan, blue). The inset shows a similar plot for the three-site ring exchange K by itself. The dark yellow background indicates the area, where the CSL is observed within ED and VMC, whereas the light yellow corresponds to its prediction in only VMC both for the fifth-order effective model.

can be written as functions of t/U and Φ and can in principle be used for the whole phase diagram. Since they are rational functions though, unphysical divergencies emerge at certain points. In the area around such a point one has to use the bare series. In this respect we found a composition of $[3,2]$ -Padé extrapolations for E_0 , J and K , $[2,1]$ -Padé extrapolations for $L_s^{2\text{sp}}$, $L_d^{2\text{sp}}$, $L_s^{3\text{sp}}$, $L_d^{3\text{sp}}$ and $L_r^{4\text{sp}}$, and all other couplings as bare series to work best for the flux $\Phi = \pi$. For this point, similar to Fig. 3 of the main article, the largest coupling constants of every

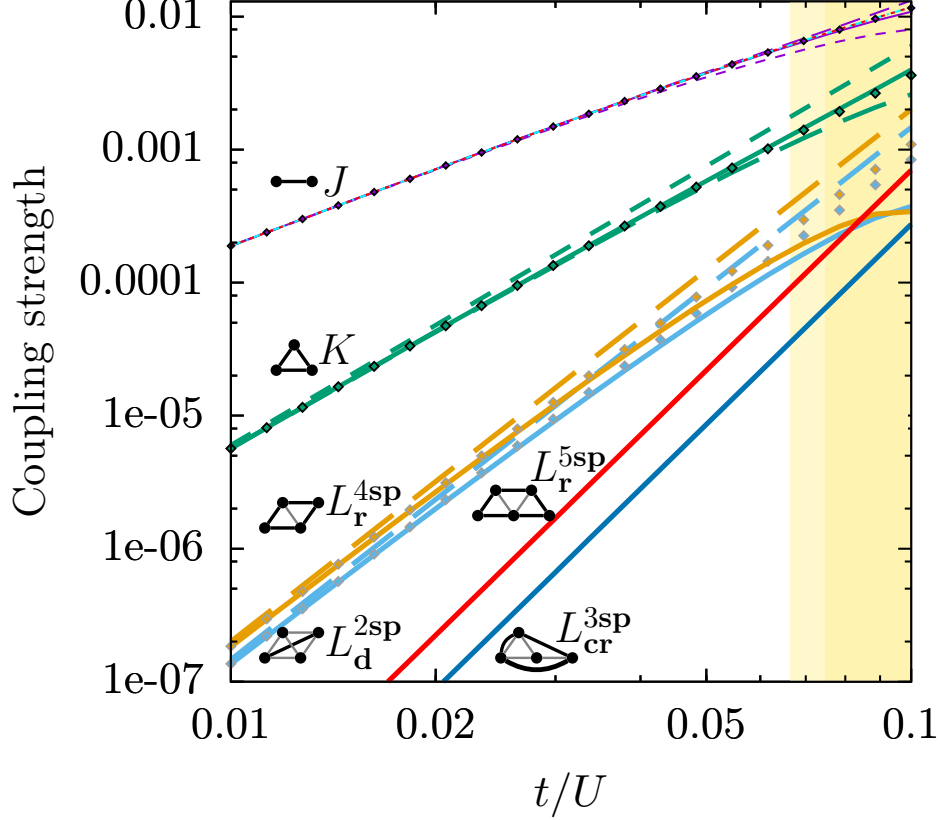


FIG. S2. Effective couplings in units of U of the Hubbard model as a function of t/U for $\Phi = \pi$ in a double logarithmic plot. Shown are the largest contributions in every order with a pictogram sketching the associated permutations. The bare fifth- (solid line), fourth- (long dashes) and third-order (short dashes) series as well as [3,2]- and [2,1]-Padé extrapolations (diamonds encircled in black and gray respectively) are indicated. For the nearest-neighbor exchange the [2,2]- and [2,3]-Padé extrapolations (red and cyan dashed lines) are given as well. The background colors can be understood as in Fig. S1.

order are shown as bare fifth-, fourth- and third-order series (full, long dashes, short dashes) and if possible as Padé extrapolations (mostly diamonds) in a double logarithmic plot in Fig. S2. This representation directly indicates the leading orders and allows to extract the ratios of t/U where higher-order contributions become influential. Note that Padé extrapolations of series starting only in higher orders can not be calculated directly, when the exponent of the numerator is smaller than the starting order of the series. This can be resolved by considering the series in units of (t/U) or (t^2/U^2) for the extrapolation. For intermediate values of the flux Φ divergencies appear for the coupling constant L_d^{2sp} around $\Phi \approx 0.6\pi$ and for L_s^{3sp} around $\Phi \approx 0.55\pi$ and $\Phi \approx 0.75\pi$ depending on t/U . Here one also has to use the bare series. However, for $\Phi = \pi/2$ the set-up of extrapolations as described for $\Phi = \pi$ works. Since we also see the signature of the CSL phase in this area, we show the convergence behavior for $\Phi = \pi/2$ in Fig. S3 and Fig. S4. For this special case a number of interesting and subtle features of the model become clear, which we discuss in the following. Note at first that the three-site ring exchange K is purely imaginary only in order three. The fourth-order term partly arises from fluctuations around two triangles leading to a flux of 2Φ , therefore a real part is present in higher orders. Similarly, the imaginary part of the fourth-order contribution to the four-site ring exchange vanishes and it effectively becomes an order five term. As a consequence the model is dominated by a real nearest-neighbor and an imaginary three-site ring exchange. For exactly this subset of interactions the CSL phase was found in [21]. The ratios of Padé extrapolants for the imaginary part of $-K$ and the real quantity J (green) and the direct Padé extrapolation of the ratio $-\text{Im}K/J$ (black) are shown in Fig. S4. We see that in the regime of interest in t/U not only the extrapolations, but also the bare fifth-order (solid line) series are well converged.

As we realized for $\Phi = \pi/2$, cancellation effects of different orders at specific values of the flux Φ lead to subtleties in the convergence behavior. For most parts of the phase diagram we find a good convergence by comparing the ED and VMC results in different orders. It is only in the area around $\Phi \approx 3\pi/4$ that the results between fourth- and

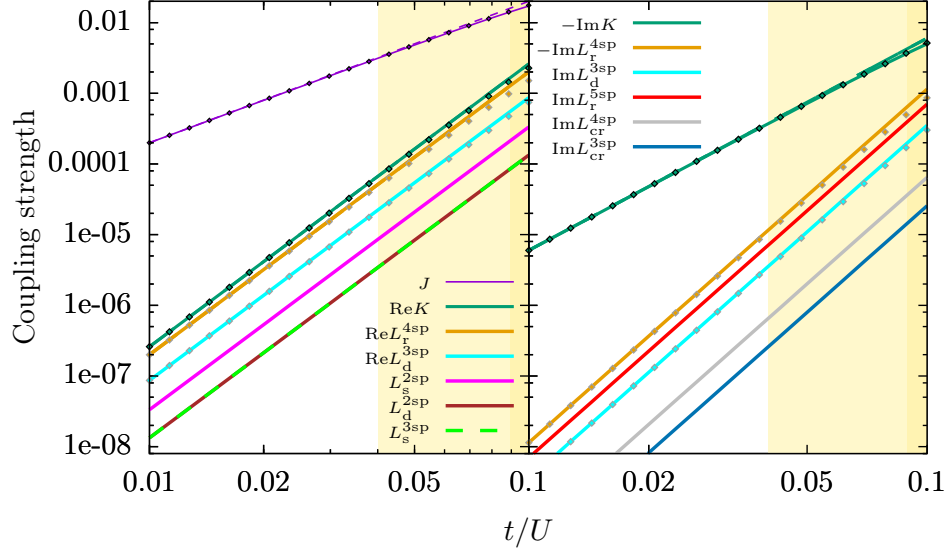


FIG. S3. Effective couplings in units of U of the Hubbard model as a function of t/U for $\Phi = \pi/2$ in a double logarithmic plot. Shown are the non-vanishing real and imaginary contributions in bare orders. The diamonds encircled in black (gray) give the Padé extrapolants with the exponents $[3,2]$ ($[2,1]$). Note, that all uneven (even) terms in the real (imaginary) part vanish. The background colors can be understood as in Fig. S1.

fifth-order change qualitatively. A possible explanation for this is the vanishing real part of the leading fourth-order ring exchange in order five, due to an alternating behavior in contrast to a large monotonic five-site ring-exchange. The interplay of these two effects arises only in order five.

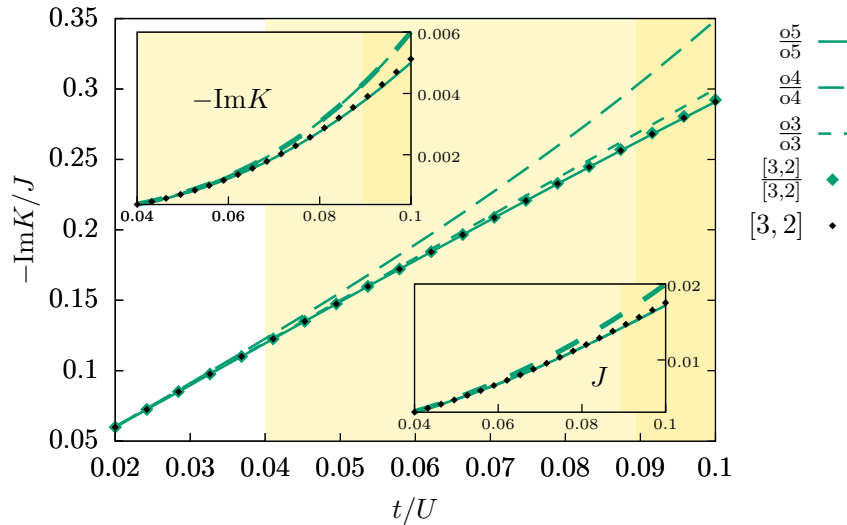


FIG. S4. Imaginary part of the ratio of effective coupling constants $-K/J$ depending on t/U for $\Phi = \pi/2$ using bare series up to order five. The ratios of Padé extrapolants with the exponents $[3,2]$ as well as the direct Padé extrapolation of the ratio $-ImK/J$ are indicated. The insets show similar plots for the imaginary part of the negative three-site ring exchange $-ImK$ and the nearest-neighbor exchange J . Extrapolations of J with different pairs of exponents $[2,2]$ and $[2,3]$ are identical at $\Phi = \pi/2$. The background colors can be understood as in Fig. S1.

COMPARISON OF ED ON THE 12- AND 21-SITE CLUSTER

In the following we give energy spectra from ED on the 12-site cluster with PBC for the comparison with the spectra from the 21-site cluster in the main article. The low-energy states of both clusters are identified by symmetry eigenvalues and corresponding states are colored in the same way. The detailed description of the symmetries is discussed below.

For the J - K model the spectrum for constant $\text{Re}K/J = 0.37$ and varying phase φ on 12 sites is shown in Fig. S5 including a zoom on the $\varphi \in [0.98\pi, \pi]$ on the right hand side. The corresponding 21 sites spectrum is shown in the left panel of Fig. 2 in the main text. Qualitatively the spectra from both clusters look very similar, since the same low-energy states and level crossings are present. The most relevant difference can be seen in the regime of the CSL phase for $0.5\pi \lesssim \varphi < \pi$. Here the energy gap between the non-degenerate ground state (blue) and the two-fold degenerate first excited state (red) with respect to the energy gap to the second excited state (green) is much smaller for the 21-site cluster in comparison to the 12-site cluster. For the special case of $\varphi = \pi$ the order of the six CSL ground states is interchanged between 12 and 21 sites. More importantly, the states of the CSL ground state manifold lie much closer together on 21 sites in comparison to 12 sites and show a larger gap to the states above.

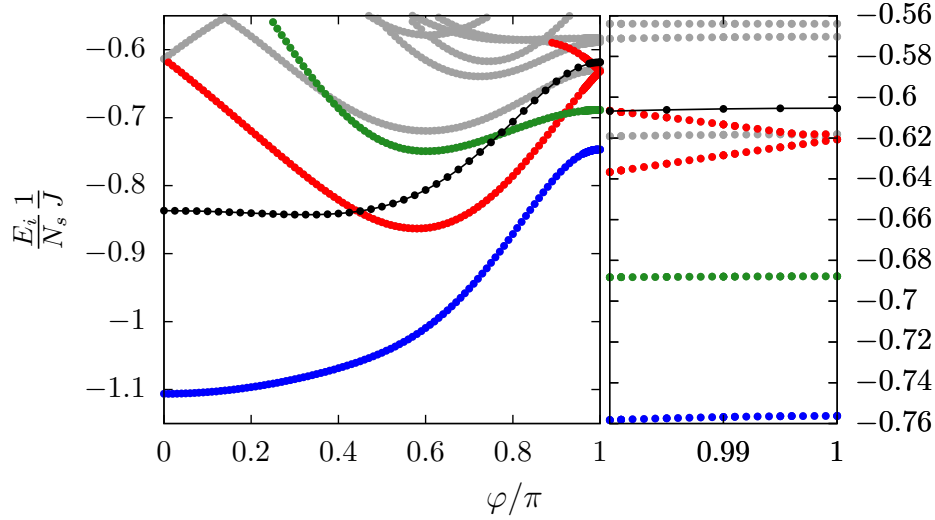


FIG. S5. Energy spectrum of the J - K model as a function of φ for fixed $\text{Re}K/J = 0.37$ from ED on a cluster with 12 sites and PBC. The right panel shows a zoom on the area close to $\varphi = \pi$. The energies from the eight-dimensional irrep **8** are illustrated in black, whereas all other colors belong to the singlet sector. The colors of the chiral states signify the same degeneracies and symmetries as in the main text and are specified in the symmetry section of these Supplementary Materials.

The spectrum of the J - K model at $\varphi = \pi$ and of the effective spin model at $\Phi = \pi$ for 12 sites are shown in the left and right panel of Fig. S6 respectively. The spectra for corresponding parameters for the 21-site cluster are given in Fig. 4 of the main text. Again the same six low-energy states occur on both clusters. In contrast to the 21-site cluster they are intertwined on 12 sites by one other state, hence the signature of the CSL phase breaking time-reversal symmetry spontaneously becomes clearer with increasing system size.

VMC PHASE DIAGRAM FOR 36 SITES

Here we give a detailed list of the different variational states we considered for the phase diagram shown in Fig. 1. of the main text, and the variational parameters in each case. We start from a nearest-neighbor non-interacting model

$$\mathcal{H}_\alpha = - \sum_{\langle i,j \rangle} \left(t_{i,j}^\alpha c_{i,\alpha}^\dagger c_{j,\alpha} + \text{h.c.} \right) + \sum_i \mu_{i,\alpha} c_{i,\alpha}^\dagger c_{i,\alpha}, \quad (\text{S10})$$

where α denotes the color, and $c_{i,\alpha}^\dagger (c_{i,\alpha})$ is a creation(annihilation) operator of an α -fermion on site i . For each color we fill the one-fermion states up to $1/N$ -filling in order to get an average filling of one fermion per site, then the

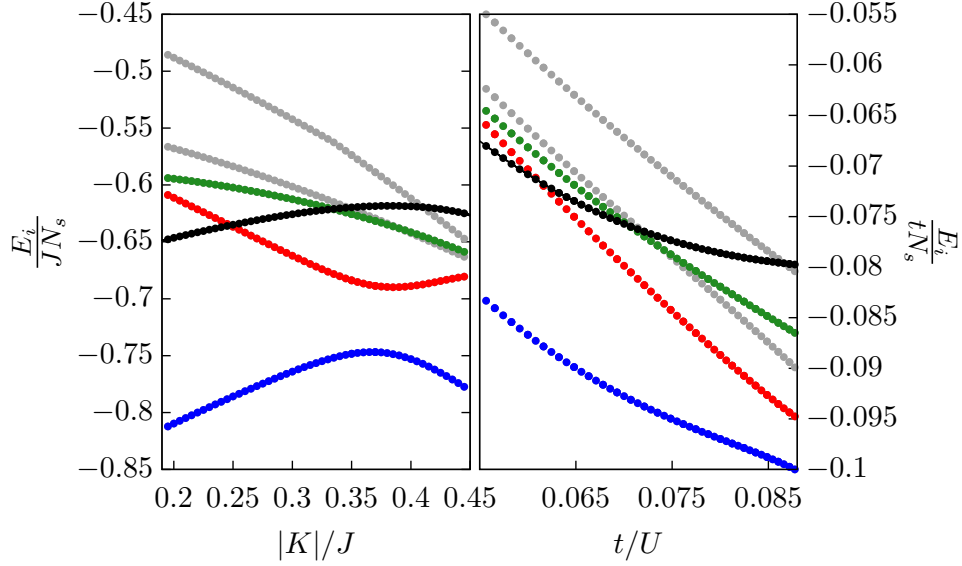


FIG. S6. The left panel shows the energy spectrum of the J - K model as a function of $\text{Re}K/J$ for fixed $\varphi = \pi$ from ED on a cluster with 12 sites and PBC. The right panel gives the corresponding spectrum of the effective spin model for $\Phi = \pi$ and varying t/U . The notation is the same as in Fig. S5.

Gutzwiller projection excludes the charge fluctuations and guarantees the strict one fermion per site filling.

Chiral spin liquid states— To create spin liquid variational states, we set all the $\mu_{i,\alpha}$ onsite terms to zero, and the $t_{i,j}^\alpha$ hopping amplitudes to unit magnitude. The phases of the hopping amplitudes are set up using the string gauge [21, 41], so that the total phase or flux on every triangular plaquette is the same. We considered the cases with $k\pi/6$ -flux ($k \in \mathbb{Z}$) per plaquette. We also made calculations on states with opposite fluxes on up and down triangles with fluxes $\pm k\pi/3$.

Plaquette ordered states— By increasing the magnitude of the hopping amplitudes around distinct triangles in Eq. (S10) we can create variational states with stronger bonds around these triangles. We considered all the possible plaquette coverings on the 36-site system, with a uniform zero- or π -flux per plaquette, changing the magnitude of hoppings around the plaquettes from 0.5 to 2 (the magnitude of the other hopping amplitudes were set to 1). In the special case of the all-up plaquette covering (shown in Fig. S7) we considered additional flux configurations with either zero- or π -flux per plaquette for each of the three different types of triangles, respectively (up triangles with 3 strong bonds, down triangles with 1 strong bond, up triangles with no strong bond). We also checked the all-up plaquette order with a uniform $k\pi/6$ -flux ($k \in \mathbb{Z}$) per plaquette.

Color order — If the chemical potentials are different for different colors, the resulting variational states will have $\text{SU}(N)$ symmetry breaking color order. We considered states with a three-sublattice color order as shown in Fig. S7, by setting $-2 \leq \mu_{i,\alpha} < 0$ on sublattice α . We combined this color order with the all-up plaquette order of the previous point, changing two variational parameters simultaneously. We made such calculations for each of the uniform $k\pi/6$ -flux ($k \in \mathbb{Z}$) cases.

Winners— Among all the above scenarios, we found three cases to be present in the phase diagram of the $J - K$ model. The three-sublattice color-ordered state with 0-flux per plaquette appears around the $K = 0$ nearest-neighbor Heisenberg model and in the area where $\text{Re}K/J < 0$ and $\varphi < \pi/2$. For values $\text{Re}K/J > 0$ and $\varphi > \pi/2$ the $\pi/3$ -flux per plaquette CSL state becomes the lowest in energy, as discussed in the main text. We also found signs of a different, $2\pi/3$ -flux CSL for large $K/J \gtrsim 1.2$ on the $\varphi > 3\pi/4$ side of the phase diagram (see Fig. S8). A similar phase was reported by Lai [19] for $K/J \gtrsim 6$ at $\varphi = \pi$ using mean-field methods.

CHIRAL STATES

The signature of the chiral states at $\Phi = \pi$ is explained in detail in the main text, where we identified states between ED and VMC as well as on different clusters by the symmetries of the states. Here we define the symmetry operators and give the eigenvalues of the chiral states.

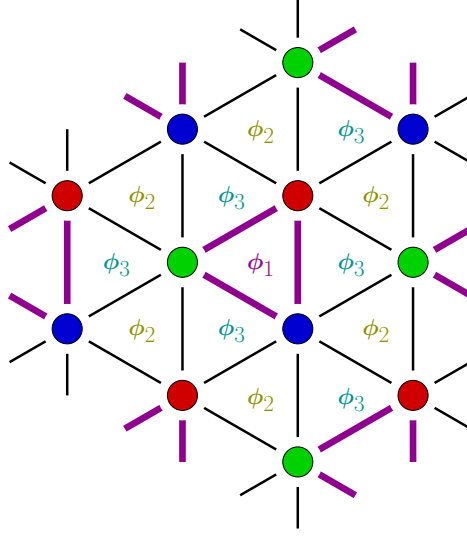


FIG. S7. Illustration for the considered hopping configurations in the VMC calculations. The magnitude of the hopping amplitudes on the thick purple bonds were changed between 0.5 and 2, while an onsite chemical potential corresponding to the three-sublattice order was changed from 0 to -2 , the ϕ_1, ϕ_2, ϕ_3 phases were either chosen to be uniform with values $k\pi/6$, or set to 0 or π respectively.

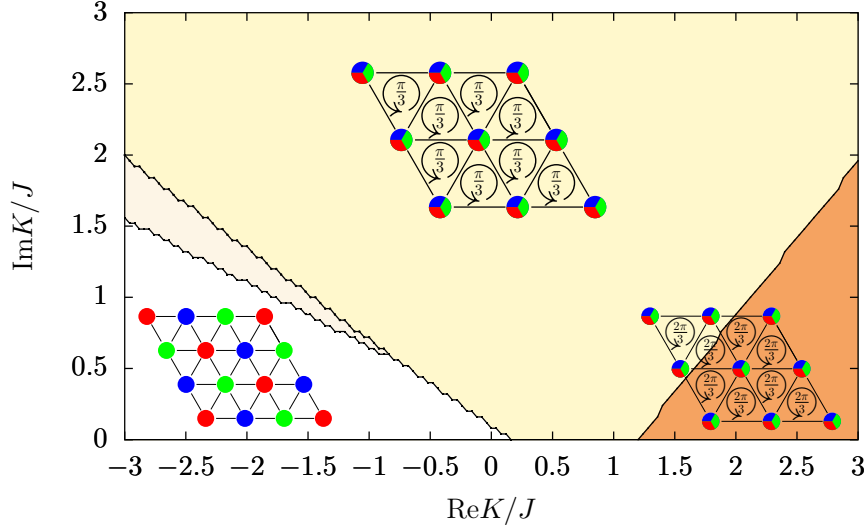


FIG. S8. The phase diagram of the J - K model for complex phases φ between zero and π for larger values of $\text{Re}K/J$ derived by VMC. A zoomed in version focusing on physically more relevant small values of $\text{Re}K/J$ is shown in Fig. 1 of the main text. For $\text{Re}K/J > 1.2$ and for φ close to π we find a $2\pi/3$ -flux chiral phase (brown). The region (light yellow) between the 3-sublattice long range ordered (white) and the $\pi/3$ -flux chiral phase (light orange) corresponds to variational states with long-range order and $\pi/6$ -flux through each triangular plaquette. We believe that it is only a result of the finite resolution of the variational parameters, as the area shrunk once we took a denser sweep.

Let the lattice constant be a and the lattice vectors $\vec{r}_1 = (a, 0)$ and $\vec{r}_2 = a(\cos(\pi/3), \sin(\pi/3))$. Then the translation operator T_1 (T_2) is defined by a translation along \vec{r}_1 (\vec{r}_2). Furthermore, we define a rotation operator $R_{\pi/3}$, which rotates counterclockwise by an angle $\pi/3$. Note that translations and rotation do not have a joint eigenbasis and we mark the eigenstates of H and $R_{\pi/3}$ with a star. The eigenvalues for the six chiral states at the flux value $\Phi = \pi$ are given in Tab. II, III and IV. Away from the $\Phi = \pi$ point the $|\Psi_2^*\rangle$ and $|\Psi_3^*\rangle$ states belong to complex one-dimensional irreducible representations of the C_6 group, but they are degenerate due to the equivalence of the K and K' points in

the Brillouin zone. Similarly, $|\Psi_5^*\rangle$ and $|\Psi_6^*\rangle$ are degenerate. At $\Phi = \pi$ these four states become degenerate due to the restored time-reversal symmetry, at this point $|\Psi_2^*\rangle$ and $|\Psi_5^*\rangle$ form a pair corresponding to the two-dimensional real E_2 irreducible representation of C_6 , while $|\Psi_3^*\rangle$ and $|\Psi_6^*\rangle$ form a pair corresponding to the two-dimensional real E_1 irreducible representation. Note that for the 21-site cluster the $|\Psi_1\rangle$ and $|\Psi_4\rangle$ states belong to the one-dimensional B irrep of C_6 , while for 12 sites they belong to the A irrep, which is an artifact of the different cluster geometries.

With VMC we calculated the symmetry properties of the chiral states for larger clusters as well. For systems where the vectors defining the torus lie in the \vec{r}_1 and \vec{r}_2 directions all six chiral states have a wave vector zero. The smallest such example is the 36-site cluster for which we provide the symmetry properties in Tab. IV. For this case, all six states are non-degenerate if $\Phi \neq \pi$. For $\Phi = \pi$ a pair of states becomes degenerate, and the rest remain non-degenerate.

As an additional information we give the phase transition points in ED and VMC on 21 sites at $\Phi = \pi/2$. With ED we find $t/U|_c^{\mathcal{O}(3),\text{ED}} \approx t/U|_c^{\mathcal{O}(5),\text{ED}} \approx 0.09$ for the third- and fifth-order effective model. In VMC the values are smaller $t/U|_c^{\mathcal{O}(3),\text{VMC}} \approx t/U|_c^{\mathcal{O}(5),\text{VMC}} \approx 0.04$. This is plausible, since the VMC captures CSL phases more naturally than long-range ordered phases and one expects the corresponding energies to minimize better.

	$ \Psi_1\rangle$	$ \Psi_2\rangle$	$ \Psi_3\rangle$	$ \Psi_4\rangle$	$ \Psi_5\rangle$	$ \Psi_6\rangle$
t_1	1	$e^{-i2\pi/3}$	$e^{i2\pi/3}$	1	$e^{-i2\pi/3}$	$e^{i2\pi/3}$
t_2	1	$e^{i2\pi/3}$	$e^{-i2\pi/3}$	1	$e^{i2\pi/3}$	$e^{-i2\pi/3}$
	$ \Psi_1\rangle$	$ \Psi_2^*\rangle$	$ \Psi_3^*\rangle$	$ \Psi_4\rangle$	$ \Psi_5^*\rangle$	$ \Psi_6^*\rangle$
$r_{\pi/3}$	1	$e^{-i2\pi/3}$	$e^{i\pi/3}$	1	$e^{i2\pi/3}$	$e^{-i\pi/3}$

TABLE II. Eigenvalues of symmetry operators for the six chiral states $|\Psi_i\rangle$ or $|\Psi_i^*\rangle$ ($|\Psi_1\rangle$ is the ground state, $|\Psi_2\rangle$ and $|\Psi_3\rangle$ are the first-excited states, etc.) for the 12-site cluster at $\Phi = \pi$. The states $|\Psi_2\rangle$ and $|\Psi_3\rangle$ as well as $|\Psi_5\rangle$ and $|\Psi_6\rangle$ are degenerate on 12 sites. The eigenvalues $t_1(t_2)$ correspond to a translation along $(a, 0)$ ($a(\cos(\pi/3), \sin(\pi/3))$) with the lattice constant a . The eigenstates denoted without (with) a star are diagonalized in the joint eigenbasis between the Hamiltonian and the translation (rotation) operator

	$ \Psi_1\rangle$	$ \Psi_2\rangle$	$ \Psi_3\rangle$	$ \Psi_4\rangle$	$ \Psi_5\rangle$	$ \Psi_6\rangle$
t_1	1	$e^{-i2\pi/3}$	$e^{i2\pi/3}$	1	$e^{-i2\pi/3}$	$e^{i2\pi/3}$
t_2	1	$e^{i2\pi/3}$	$e^{-i2\pi/3}$	1	$e^{i2\pi/3}$	$e^{-i2\pi/3}$
	$ \Psi_1\rangle$	$ \Psi_2^*\rangle$	$ \Psi_3^*\rangle$	$ \Psi_4\rangle$	$ \Psi_5^*\rangle$	$ \Psi_6^*\rangle$
$r_{\pi/3}$	-1	$e^{-i2\pi/3}$	$e^{i\pi/3}$	-1	$e^{i2\pi/3}$	$e^{-i\pi/3}$

TABLE III. Eigenvalues of symmetry operators for the six chiral states for the 21-site cluster at $\Phi = \pi$. The notation is as in Tab. II. The degeneracies on 12 and 21 sites are identical.

	$ \Psi_1\rangle$	$ \Psi_2\rangle$	$ \Psi_3\rangle$	$ \Psi_4\rangle$	$ \Psi_5\rangle$	$ \Psi_6\rangle$
t_1, t_2	1	1	1	1	1	1
$r_{\pi/3}$	1	1	$e^{-i2\pi/3}$	$e^{i2\pi/3}$	-1	-1
irrep of D_6	A_1	A_2	E_2		B_2	B_1

TABLE IV. Eigenvalues of symmetry operators for the six chiral states for the 36-site cluster at $\Phi = \pi$. The notation is similar to Tab. II. On 36 sites the states $|\Psi_3\rangle$ and $|\Psi_4\rangle$ are degenerate, while the others are non-degenerate.

* carolin.boos@fau.de
† miklos.lajko@epfl.ch
‡ pnataf@ethz.ch
§ penc.karlo@wigner.mta.hu
¶ kai.phillip.schmidt@fau.de
** frederic.mila@epfl.ch

[1] C. Nayak, S. H. Simon, A. Stern, M. Freedman, and S. Das Sarma, *Rev. Mod. Phys.* **80**, 1083 (2008).

- [2] I. Bloch, *Nature Physics* **1**, 23 (2005).
- [3] U. Schneider, L. Hackermüller, S. Will, T. Best, I. Bloch, T. A. Costi, R. W. Helmes, D. Rasch, and A. Rosch, *Science* **322**, 1520 (2008), <http://science.sciencemag.org/content/322/5907/1520.full.pdf>.
- [4] S. Taie, R. Yamazaki, S. Sugawa, and Y. Takahashi, *Nature Physics* **8**, 825 (2012).
- [5] C. Hofrichter, L. Riegger, F. Scazza, M. Höfer, D. R. Fernandes, I. Bloch, and S. Fölling, *Phys. Rev. X* **6**, 021030 (2016).
- [6] M. Aidelsburger, M. Atala, M. Lohse, J. T. Barreiro, B. Paredes, and I. Bloch, *Phys. Rev. Lett.* **111**, 185301 (2013).
- [7] H. Miyake, G. A. Siviloglou, C. J. Kennedy, W. C. Burton, and W. Ketterle, *Phys. Rev. Lett.* **111**, 185302 (2013).
- [8] M. A. Cazalilla, A. F. Ho, and M. Ueda, *New Journal of Physics* **11**, 103033 (2009).
- [9] A. V. Gorshkov, M. Hermele, V. Gurarie, C. Xu, P. S. Julienne, J. Ye, P. Zoller, E. Demler, M. D. Lukin, and A. M. Rey, *Nature Physics* **6**, 289 (2010).
- [10] F. Scazza, C. Hofrichter, M. Höfer, P. C. De Groot, I. Bloch, and S. Fölling, *Nature Physics* **10**, 779 (2014).
- [11] X. Zhang, M. Bishof, S. L. Bromley, C. V. Kraus, M. S. Safronova, P. Zoller, A. M. Rey, and J. Ye, *Science* **345**, 1467 (2014), <http://science.sciencemag.org/content/345/6203/1467.full.pdf>.
- [12] M. A. Cazalilla and A. M. Rey, *Reports on Progress in Physics* **77**, 124401 (2014).
- [13] M. Hermele, V. Gurarie, and A. M. Rey, *Phys. Rev. Lett.* **103**, 135301 (2009).
- [14] Y.-C. He, D. N. Sheng, and Y. Chen, *Phys. Rev. Lett.* **112**, 137202 (2014).
- [15] W.-J. Hu, W. Zhu, Y. Zhang, S. Gong, F. Becca, and D. N. Sheng, *Phys. Rev. B* **91**, 041124 (2015).
- [16] A. Wietek, A. Sterdyniak, and A. M. Läuchli, *Phys. Rev. B* **92**, 125122 (2015).
- [17] M. Hermele and V. Gurarie, *Phys. Rev. B* **84**, 174441 (2011).
- [18] S. Bieri, M. Serbyn, T. Senthil, and P. A. Lee, *Phys. Rev. B* **86**, 224409 (2012).
- [19] H.-H. Lai, *Phys. Rev. B* **87**, 205111 (2013).
- [20] H.-H. Lai, *Phys. Rev. B* **87**, 205131 (2013).
- [21] P. Nataf, M. Lajkó, A. Wietek, K. Penc, F. Mila, and A. M. Läuchli, *Phys. Rev. Lett.* **117**, 167202 (2016).
- [22] H. Tsunetsugu and M. Arikawa, *Journal of the Physical Society of Japan* **75**, 083701 (2006), <https://doi.org/10.1143/JPSJ.75.083701>.
- [23] B. Bauer, P. Corboz, A. M. Läuchli, L. Messio, K. Penc, M. Troyer, and F. Mila, *Phys. Rev. B* **85**, 125116 (2012).
- [24] P. Nataf and F. Mila, *Phys. Rev. Lett.* **113**, 127204 (2014).
- [25] H. Yokoyama and H. Shiba, *J. Phys. Soc. Jpn.* **56**, 1490 (1987).
- [26] C. Gros, *Annals of Physics* **189**, 53 (1989).
- [27] P. Corboz, M. Lajkó, A. M. Läuchli, K. Penc, and F. Mila, *Phys. Rev. X* **2**, 041013 (2012).
- [28] Y. Iqbal, F. Becca, and D. Poilblanc, *Phys. Rev. B* **84**, 020407 (2011).
- [29] W.-J. Hu, W. Zhu, Y. Zhang, S. Gong, F. Becca, and D. N. Sheng, *Phys. Rev. B* **91**, 041124 (2015).
- [30] Y. Zhang, T. Grover, A. Turner, M. Oshikawa, and A. Vishwanath, *Phys. Rev. B* **85**, 235151 (2012).
- [31] A. Wietek, A. Sterdyniak, and A. M. Läuchli, *Phys. Rev. B* **92**, 125122 (2015).
- [32] B. Bernu, C. Lhuillier, and L. Pierre, *Phys. Rev. Lett.* **69**, 2590 (1992).
- [33] A. Läuchli, F. Mila, and K. Penc, *Phys. Rev. Lett.* **97**, 087205 (2006).
- [34] K. Coester and K. P. Schmidt, *Phys. Rev. E* **92**, 022118 (2015).
- [35] T. Kato, *Phys. Rev.* **77**, 413 (1950).
- [36] M. Takahashi, *Journal of Physics C: Solid State Physics* **10**, 1289 (1977).
- [37] A. H. MacDonald, S. M. Girvin, and D. Yoshioka, *Phys. Rev. B* **37**, 9753 (1988).
- [38] E. Müller-Hartmann and A. Reischl, *Eur. Phys. J. B* **28**, 173 (2002).
- [39] H.-Y. Yang, A. M. Läuchli, F. Mila, and K. P. Schmidt, *Phys. Rev. Lett.* **105**, 267204 (2010).
- [40] A. C. Guttman, *Phase Transitions and Critical Phenomena*, edited by C. Domb and J. Lebowitz, Vol. 13 (Academic Press, New York, 1989).
- [41] Y. Hatsugai, K. Ishibashi, and Y. Morita, *Phys. Rev. Lett.* **83**, 2246 (1999).